J. Fluid Mech. (2023), *vol.* 967, R2, doi:10.1017/jfm.2023.497

JFM RAPIDS

Towards decoupling the effects of permeability and roughness on turbulent boundary layers

D.D. Wangsawijaya[1,†], **P. Jaiswal**[1] **and B. Ganapathisubramani**[1]

[1]Aeronautical and Astronautical Engineering, University of Southampton, Southampton SO17 1BJ, UK

(Received 1 March 2023; revised 9 May 2023; accepted 13 June 2023)

Boundary-layer flow over a realistic porous wall might contain both the effects of wall-permeability and wall-roughness. These two effects are typically examined in the context of a rough-wall flow, i.e. by defining a 'roughness' length or equivalent to capture the effect of the surface on momentum deficit/drag. In this work, we examine the hypothesis of Esteban *et al.* (*Phys. Rev. Fluids*, vol. 7, no. 9, 2022, 094603), that a turbulent boundary layer over a porous wall could be modelled as a superposition of the roughness effects on the permeability effects by using independently obtained information on permeability and roughness. We carry out wind tunnel experiments at high Reynolds number ($14\,400 \leq Re_\tau \leq 33\,100$) on various combinations of porous walls where different roughnesses are overlaid over a given permeable wall. Measurements are also conducted on the permeable wall as well as the rough walls independently to obtain the corresponding length scales. Analysis of mean flow data across all these measurements suggests that an empirical formulation can be obtained where the momentum deficit (ΔU^+) is modelled as a combination of independently obtained roughness and permeability length scales. This formulation assumes the presence of outer-layer similarity across these different surfaces, which is shown to be valid at high Reynolds numbers. Finally, this decoupling approach is equivalent to the area-weighted power-mean of the respective permeability and roughness length scales, consistent with the approach recently suggested by Hutchins *et al.* (*Ocean Engng*, vol. 271, 2023, 113454) to capture the effects of heterogeneous rough surfaces.

Key words: turbulent boundary layers

1. Introduction

Flow over porous walls comprises an extensive number of natural phenomena, ranging from blood vessels to the atmospheric boundary layer (ABL) developing over a

† Email address for correspondence: D.D.Wangsawijaya@soton.ac.uk

© The Author(s), 2023. Published by Cambridge University Press. This is an Open Access article, distributed under the terms of the Creative Commons Attribution licence (http://creativecommons.org/licenses/by/4.0), which permits unrestricted re-use, distribution and reproduction, provided the original article is properly cited.

https://doi.org/10.1017/jfm.2023.497 Published online by Cambridge University Press

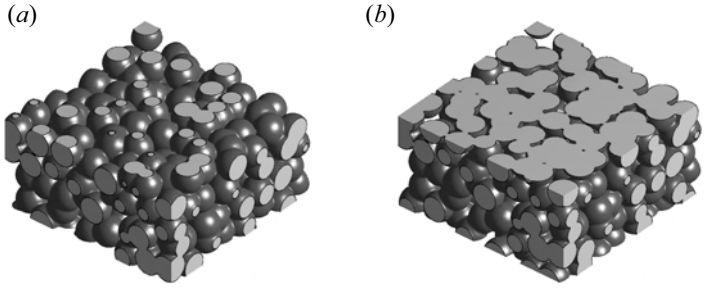

Figure 1. Illustrations of realistic permeable walls with roughness interfaces: (*a*) positive and (*b*) negative skewnesses. Adapted from Rosti, Cortelezzi & Quadrio (2015).

forest canopy. The latter can be considered as a turbulent boundary layer (TBL) developing over a porous wall. An example of porous walls, constructed from packed spheres, is shown in figure 1. Here, both walls approximately have the same permeability (i.e. the inverse of resistance of a substrate to fluid flows) and some form of roughness: the wall shown in figure 1(*a*) has roughness protrusions (positive skewness) above the porous wall, while in figure 1(*b*) this roughness interface comprises recesses (negative skewness). Thus, a realistic representation of a porous wall is both permeable and rough to some extent, and the effects of both permeability and roughness have to be considered for characterisation of a TBL developing over such wall.

1.1. *Rough walls*

The presence of rough walls increases skin friction from that of smooth walls and thus the time-averaged streamwise velocity of TBLs developing over rough walls (U_r^+, subscript 'r' denotes a rough wall; y, wall-normal location) can be written as a downward shift of the logarithmic region from the smooth wall velocity profile:

$$U_r^+ = \frac{1}{\kappa}\ln\left[\frac{(y+d)U_\tau}{\nu}\right] + B - \Delta U_r^+ = \frac{1}{\kappa}\ln(y+d)^+ + B - \Delta U_r^+. \tag{1.1}$$

The viscous-scaled velocity is defined as $U_r^+ \equiv U_r/U_\tau$, where $U_\tau \equiv \sqrt{\tau_w/\rho}$ is the friction velocity, τ_w and ρ are the wall shear stress (WSS) and the density of fluid, respectively. The logarithmic profile is defined as follows: κ is the von Kármán constant, d is the zero-plane displacement, ν is the kinematic viscosity of fluid, and B is the log-law intercept. In the fully rough regime, the logarithmic shift ΔU_r^+, also known as the Hama roughness function (Hama 1954), is defined as

$$\Delta U_r^+ = \frac{1}{\kappa}\ln\left(\frac{k_{s_r}U_\tau}{\nu}\right) + B - B_{FR} = \frac{1}{\kappa}\ln k_{s_r}^+ + B - B_{FR}, \tag{1.2}$$

where k_{s_r} is the equivalent sand grain roughness of a rough wall (note that we use different subscripts throughout this study to distinguish the equivalent sand grain roughness between different test surfaces: subscripts 'r' for rough, 'p' for porous, and 'pr' for porous–rough walls) and $B_{FR} = 8.5$ is the 'fully' rough intercept of the velocity profile of sand grain roughness. It should be noted that the 'equivalent sand grain roughness' is a measure of roughness effect on the flow relative to that of a uniform sand grain roughness (Nikuradse 1933); it can only be determined by flow measurements. The mean streamwise

https://doi.org/10.1017/jfm.2023.497 Published online by Cambridge University Press

velocity profile of a rough wall in fully rough regime can therefore be written as a function of its equivalent sand grain roughness:

$$U_r^+ = \frac{1}{\kappa} \ln\left(\frac{y+d}{k_{s_r}}\right) + B_{FR}. \tag{1.3}$$

1.2. *Permeable walls*

Earlier studies of TBLs developing over permeable walls involved various types of such walls, namely: packed spheres (Zagni & Smith 1976), perforated sheets (Kong & Schetz 1982), bed of grains (Zippe & Graf 1983) and multi-layered walls (Manes *et al.* 2009). Permeable walls have been found to increase drag (i.e. skin friction coefficient $C_f \equiv 2(U_\tau/U_\infty)^2$, where U_∞ is the free stream velocity) from that of solid, impermeable walls, which is attributed to the increase of dissipation, momentum flux and Reynolds shear stress on the interface between the fluid and the substrates (Zagni & Smith 1976; Shimizu, Tsujimoto & Nakagawa 1990). Similar to the rough-wall TBLs, the increase in C_f of permeable walls is also characterised by a downward shift in the logarithmic region from that of a solid, smooth wall (Hahn, Je & Choi 2002; Efstathiou & Luhar 2018). Thus, it is probable that there is a 'universal' parameter that characterises permeable walls – possibly equivalent to the equivalent sand grain roughness for rough-wall TBLs. It was suggested by Manes, Poggi & Ridolfi (2011) that the logarithmic region of a TBL developing over a permeable wall scales on permeability K:

$$U_p^+ = \frac{1}{\kappa} \ln\left(\frac{y+d}{\sqrt{K}}\right) + c_1, \tag{1.4}$$

where U_p is the time-averaged streamwise velocity of a TBL developing over a porous wall (subscript 'p' denotes porous wall). Previous studies observed a wide range of magnitude of κ (Breugem, Boersma & Uittenbogaard 2006; Suga *et al.* 2010; Manes *et al.* 2011), which is largely attributed to the low Re at which these studies were conducted and thus there was not enough separation between the inner and outer layers of the wall-bounded flows (Manes *et al.* 2011). A more recent experimental work by Esteban *et al.* (2022), conducted at a higher order of magnitude of Re ($2000 \leq Re_\tau \leq 18\,000$) observed that $\kappa = 0.39$, similar to that of smooth and rough-wall TBLs. It was further hypothesised by Esteban *et al.* (2022) that c_1 in (1.4) is an additive constant related to the blockage effect of a porous substrate, as a realistic porous wall comprises both permeable matrix and solid substrates (see, for example, figure 1), whose size does not permit the full isolation of permeability effect (Breugem *et al.* 2006). This blockage refers to the baseline drag incurred by the frontal area of a porous substrate and it might be represented by a roughness function similar to that of (1.2):

$$c_1 = B - \Delta U_b^+ = B - \left(\frac{1}{\kappa} \ln k_{s_b}^+ + B - B_{FR}\right), \tag{1.5}$$

where ΔU_b^+ and k_{s_b} are the downward logarithmic shift and the equivalent sand grain roughness due to the blockage of the porous substrate, respectively (subscript 'b' denotes 'blockage'). Inserting (1.5) to (1.4) yields

$$U_p^+ = \frac{1}{\kappa} \ln\left(\frac{y+d}{\sqrt{K}}\right) - \frac{1}{\kappa} \ln k_{s_b}^+ + B_{FR} = \frac{1}{\kappa} \ln\left(\frac{y+d}{Re_K k_{s_b}}\right) + B_{FR}, \tag{1.6}$$

where the Reynolds number based on surface permeability, $Re_K \equiv \sqrt{K} U_\tau/\nu$. By comparing (1.3) and (1.6), the 'equivalent sand grain roughness' of a porous wall can

https://doi.org/10.1017/jfm.2023.497 Published online by Cambridge University Press

be defined as

$$k_{s_p} = Re_K k_{s_b}. \tag{1.7}$$

We note that the characterisation for porous-wall TBLs proposed in this study (using the framework for rough-wall TBLs) has substantial similarities with that of TBLs and the atmospheric surface layer developing over vegetation (aquatic and terrestrial) canopies. Here, the 'roughness length' z_0 (Raupach 1992) is akin to k_s. Further, it has been suggested that the vegetation canopy drag coefficient C_D is determined by various canopy parameters, including but not limited to the canopy solidity, porosity, and its morphology: canopy height, blade width, stem diameter (akin to the porous substrate size in this study) and the frontal area (Luhar, Rominger & Nepf 2008; Tanino & Nepf 2008).

In this study, we take the first steps towards exploring the possibility of decoupling permeability and roughness effects on TBLs. We have constructed three different porous test surfaces where we maintain the permeability (Re_K) but the blockage is systematically altered by adding roughness onto a given permeable substrate. Detailed hot-wire and drag-balance measurements are taken for the permeable, rough and the combination of permeable–rough surfaces over a wide range of Reynolds numbers (ensuring the flow is in fully rough regime for all cases). We use the experimental data to explore two different approaches for decoupling the two effects. First, we extend the above-mentioned framework to include the effects of additional roughness. Second, we use a power-mean averaging approach proposed for heterogeneous roughness (Hutchins *et al.* 2023) to find an equivalent roughness length scale that can capture the combined effect of permeability and roughness.

2. Experimental set-up

2.1. *Facility*

Measurements are conducted inside the closed return boundary-layer wind tunnel (BLWT) at the University of Southampton. The flow passes through a contraction section of 6 : 1 ratio before entering the 12 m × 1.2 m × 1 m (length × width × height) test section. The boundary layer develops over the floor (bottom surface) of the BLWT. A 220 mm long smooth wall ramp is installed at the end of the contraction section (figure 2(*a*)ⓐ) to match the thickness of the test surfaces. This ramp marks the inlet towards the test section of the BLWT and the streamwise datum ($x = 0$). The boundary layer is tripped by a 8.5 mm wide, 0.4 mm thick turbulator tape attached on the ramp (figure 2(*a*)ⓑ). The tunnel has the free stream turbulence level of $\sigma_{u'}/U_\infty \approx 0.1\,\%$, where $\sigma_{u'}$ is the standard deviation of streamwise turbulent fluctuation at the free stream and U_∞ is the free stream velocity. The BLWT is equipped with a water-cooled heat exchanger, maintaining the flow temperature variation of 1 % for the longest measurements ($17.76 \pm 0.16\,^\circ$C within ∼8 hours).

2.2. *Test surfaces*

Five test surfaces are constructed for this study: porous wall (denoted by '*P*', figure 2(*a*)ⓒ), two types of rough walls ('*R*1' and '*R*2', figure 2*b*,*c*), and two combinations of rough walls on top of the porous wall ('*PR*1' and '*PR*2', figure 2*b*,*c*). All test surfaces are assembled on the bottom surface of the BLWT, downstream of the ramp and trip (figure 2*a*). The ramp and test surfaces only cover the first 10.8 m long part of the test section, while the section from $x = 10.8$ m to $x = 12$ m comprises a smooth wall (figure 2*a*). All measurements are conducted at a constant x location at a range free stream velocity U_∞, corresponding

https://doi.org/10.1017/jfm.2023.497 Published online by Cambridge University Press

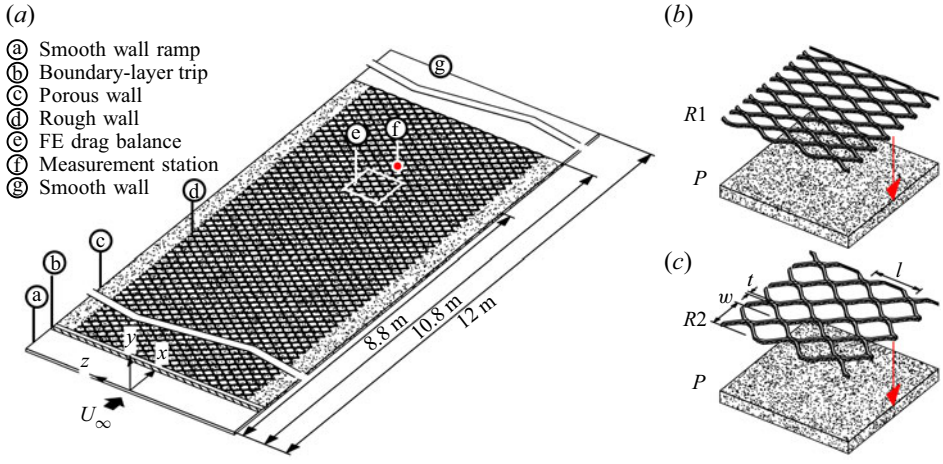

(d)

Surface	k (mm)	s (mm)	ε (–)	K ($\times 10^{-8}$ m^2)	A_o (–)	l (mm)	w (mm)	t (mm)
P	15	0.89	0.97	3.62	–	–	–	–
$R1$	3.0	–	–	–	0.73	62	30	4
$R2$	3.5	–	–	–	0.81	70	53	5

Figure 2. (*a*) Illustration of a test surface laid inside the test section of the BLWT. Combination of porous–rough test surfaces: (*b*) porous P–rough wall $R1$, and (*c*) porous P–rough wall $R2$. (*d*) Geometric parameters of P, $R1$, and $R2$, where k is the thickness of the surfaces. For P, s is the average pore size of the foam, ε is the porosity and K is the permeability, obtained from Esteban *et al.* (2022). For $R1$ and $R2$, A_o is the open area ratio of the mesh, l is the length of the longway of the mesh, w is the length of the shortway of the mesh and t is the width of the mesh strand, as illustrated in (*c*).

to a set of matched friction Reynolds number $Re_\tau \equiv \delta U_\tau/\nu \pm 1600$ (here, δ is the 99 % boundary-layer thickness) between P, $R1$ and $PR1$, as well as another set of matched Re_τ for P, $R2$ and $PR2$. The first set of test surfaces has five matched Re_τ cases ($Re_\tau \approx 14\,400$, 18 600, 23 400, 27 700 and 33 100), while the second set has four matched cases ($Re_\tau \approx$ 14 400, 18 600, 23 400 and 27 700). Details of each test surfaces, including the statistics obtained from hot-wire anemometry (HWA) and WSS measurements, are given in table 1. Throughout this study, each test surface is denoted with a symbol (see the last column in table 1). The same colour denotes surfaces with matched Re_τ and Re_K (within $Re_K \pm$ 10 %), which runs from lighter towards darker colour as Re_τ and Re_K increase.

The porous walls are constructed from sheets of 15 mm thick ($1060 \leq k^+ \equiv kU_\tau/\nu \leq$ 2130), 45 ppi (pores per inch) polyurethane reticulated foam. The substrate has the average pore size of $s = 0.89$ mm ($63 \leq s^+ \equiv sU_\tau/\nu \leq 126$) and the porosity (i.e. the ratio of empty volume over total volume) of 0.97. The porosity is comparable to that of sparse vegetation, $\varepsilon > 0.9$ (Luhar *et al.* 2008), and the pore size is higher than that of the dense canopy of Sharma & García-Mayoral (2020) ($3 \lesssim s^+ \lesssim 50$). The permeability $K = 3.62 \times 10^{-8}$ m^2, corresponding to $13 \leq Re_K \leq 27.5$ (figure 2*d*) is obtained using a 'Darcy' flow-type experiment (as in Manes *et al.* 2011 and Esteban *et al.* 2022). A sample of the porous substrate of length L and diameter D is placed inside a circular duct and subjected to an incoming air of a constant flow rate Q and dynamic viscosity μ. Pressure drop over the distance L, Δp, is obtained upstream and downstream of the porous substrate, and the permeability is defined as $K \equiv 4Q\mu L/(\pi \Delta p D^2)$. Note that unlike k_s, a quantity derived from the flow, K is obtained solely from the property of the surface.

https://doi.org/10.1017/jfm.2023.497 Published online by Cambridge University Press

Case	U_∞ (ms^{-1})	U_τ (ms^{-1})	C_f ($\times 10^{-3}$)	δ (mm)	Re_x ($\times 10^7$)	Re_τ ($\times 10^4$)	Re_K (–)	k_{s_p} (mm)	k_{s_r} (mm)	$k_{s_{pr}}$ (mm)	k_{s_b} (mm)	$k_{s_{be}}$ (mm)	Sym.
						Porous walls							
P	19.84	1.06	5.72	201.11	1.18	1.44	13.62				0.57		○
	25.45	1.36	5.74	199.96	1.52	1.85	17.57				0.45		○
	29.06	1.54	5.65	208.26	1.76	2.21	20.22	7.83	—	—	0.39	—	○
	35.46	1.87	5.59	211.27	2.14	2.72	24.50				0.32		○
	40.05	2.13	5.67	221.25	2.39	3.20	27.52				0.28		○
						Rough walls							
*R*1	14.90	0.86	6.69	232.40	0.87	1.33							△
	19.93	1.15	6.70	236.84	1.17	1.82							△
	25.20	1.46	6.67	239.38	1.48	2.32	—	—	13.52	—	—	—	△
	29.58	1.71	6.69	243.78	1.73	2.77							△
	35.21	2.04	6.69	254.33	2.05	3.42							△
*R*2	15.10	0.89	7.01	241.11	0.89	1.44							◇
	19.74	1.18	7.09	229.33	1.18	1.79	—	—	16.17	—	—	—	◇
	24.90	1.49	7.12	229.34	1.49	2.27							◇
	29.83	1.78	7.13	230.03	1.78	2.73							◇
						Porous–rough walls							
*PR*1	17.28	1.06	7.48	225.41	1.01	1.58	13.32					1.33	☆
	21.47	1.31	7.49	218.12	1.26	1.92	16.74					1.05	☆
	26.04	1.60	7.60	227.93	1.54	2.46	20.55	—	—	17.65	—	0.86	☆
	31.49	1.94	7.60	226.64	1.85	2.94	24.65					0.72	☆
	35.01	2.17	7.67	229.11	2.05	3.31	27.46					0.64	☆
*PR*2	15.06	0.95	7.94	219.42	0.90	1.41	12.27					1.59	☆
	19.97	1.26	7.93	221.73	1.20	1.91	16.40	—	—	19.45	—	1.19	☆
	25.20	1.59	7.98	224.41	1.52	2.45	20.76					0.94	☆
	28.06	1.79	8.00	222.96	1.69	2.71	23.16					0.84	☆

Table 1. Summary of all test surfaces: porous (*P*), rough (*R*1 and *R*2), and porous–rough (*PR*1 and *PR*2) walls. The statistics are obtained from HWA measurements, δ is the 99 % boundary-layer thickness. Coefficient of friction is defined as $C_f \equiv 2(U_\tau/U_\infty)^2$. Reynolds number definitions are $Re_x \equiv xU_\infty/\nu$, $Re_\tau \equiv \delta U_\tau/\nu$ and $Re_K \equiv \sqrt{K}U_\tau/\nu$. Here k_s is the equivalent sand grain roughness obtained for all test surfaces: porous (subscript '*p*'), rough ('*r*'), and porous–rough ('*pr*') walls; k_{s_b} represents the blockage of the porous substrate (1.7) and $k_{s_{be}}$ the equivalent blockage of a porous substrate with overlaying roughness (3.5). The last column shows the symbol associated with each test surface. Colours denote test cases with approximately matched Re_τ and $Re_K \approx 14\,400$ and 13 (○, yellow), 18 600 and 17 (○, orange), 23 400 and 20.5 (○, red), 27 700 and 24 (○, purple), 33 100 and 27.5 (○, black).

The rough walls are constructed from two types of diamond-shaped, expanded metal mesh sheets denoted by *R*1 and *R*2 (figure 2*b*,*c*). The mesh sheets have the thickness of $k = 3$ and 3.5 mm ($178 \leq k^+ \leq 476$) for *R*1 and *R*2, respectively, and the open area A_o (ratio of empty to total area in *xz*–plane) of 0.73 and 0.81. Both mesh sheets only cover a 1 m wide portion (in *z*) of the working section (figure 2(*a*)ⓓ).

The porous–rough walls are constructed by stacking each of the two rough walls above the porous wall (figure 2*b*,*c*). The effects of rough walls on permeability and porosity of the porous wall may be considered negligible, as the length scales of the open areas of

https://doi.org/10.1017/jfm.2023.497 Published online by Cambridge University Press

the rough walls ($O(10^1)$ mm) are two orders of magnitude higher than that of the porous wall (the pore size $O(10^{-1})$ mm). Details of the relevant parameters regarding the porous substrate and mesh geometries are given in figure 2(*d*).

2.3. *Hot-wire anemometry*

Hot-wire anemometry measurements are conducted for all test surfaces listed in table 1 by traversing the wire in the wall-normal direction y across 35–40 logarithmically spaced points from the wall towards the free stream. All measurements are conducted at the centreline of the tunnel at $x = 8.8$ m from the datum of the tunnel test section (figure 2(*a*)ⓕ). A modified Dantec 55P05 single-sensor with a boundary-layer type probe (and an appropriate probe support) are used with a StreamLine Pro constant temperature anemometer (CTA) with an overheat ratio of 0.8. The sensor is a 5 μm diameter, 1 mm long tungsten wire soldered to the tip of the hot-wire prong, satisfying the recommended wire length-to-diameter ratio of 200 (Ligrani & Bradshaw 1987) and corresponding to the viscous-scaled sensor lengths of $57 \leq l_w^+ \equiv l_w U_\tau/\nu \leq 145$. The output signal is sampled from the CTA at $f_s = 30$ kHz, yielding viscous-scaled sampling interval of $1.6 \leq t^+ \equiv U_\tau^2/(f_s\nu) \leq 10$. The sampling time T_s at each measurement point differs between test surfaces such that the boundary-layer turnover time is maintained at $T_s U_\infty/\delta \geq 20\,000$ to allow convergence of turbulence energy spectra (Hutchins *et al.* 2009). The sensor is traversed to the free stream and calibrated prior to and after each measurement. The relation between free stream velocity U_∞ and output voltage of the sensor E_∞ is defined by King's law $E_\infty^2 = C_1 + C_2 U_\infty^{C_3}$ (where C_1, C_2, and C_3 are the King's law constants). Temperature compensation is applied to the output signal to account for a slight sensor drift.

2.4. *Wall shear stress measurements*

The WSSs of all test surfaces shown in table 1 are measured using an in-house floating element (FE) drag balance. The balance has a 200 mm × 200 mm FE located at $x = 8.6$ m (figure 2(*a*)ⓒ), slightly upstream of the HWA measurement station. A section of each test surface is cut according to the size of the FE and mounted on top of the FE, leaving a 0.5 mm clearance between the FE and its housing, allowing it to move freely for WSS measurements. The housing is sealed to prevent airflow into the balance. Measurements are acquired at $f_s = 256$ Hz with 120 s sampling time for each test surface. Calibration of the balance is performed before measurements by loading a set of calibration weights to the balance via a pulley system. The relationship between known calibration weights and time-averaged output voltage from the balance is obtained by fitting the calibration data into a first-order polynomial, corresponding to the balance sensitivity of 93.15 mV g^{-1} ± 3.2 %.

Figure 3(*a*) shows the C_f of all tests surfaces as a function of fetch Reynolds number $Re_x \equiv xU_\infty/\nu$. For validation, C_f of smooth walls ($2930 \leq Re_\tau \leq 12\,500$) are determined first using three different methods: (i) direct WSS measurements using the FE drag balance (□), (ii) fitting velocity profiles obtained from HWA measurements to the composite profile of Rodríguez-López *et al.* (2015) (■), (iii) the analytical solution of Monty *et al.* (2016) (▬). All three methods show a reasonable agreement with each other within ±5 % error.

For the rest of the test surfaces *P*, *R* and *PR*, C_f are determined from direct WSS measurements. Both rough walls (*R*1 and *R*2) have higher C_f than that of porous walls, which increase further as the walls are combined with the porous walls (*PR*1 and *PR*2), as shown in figure 3(*a*). The logarithmic shift $\Delta U^+_{(p,r,pr)}$ and $k_{s_{(p,r,pr)}}$ for each of these

https://doi.org/10.1017/jfm.2023.497 Published online by Cambridge University Press

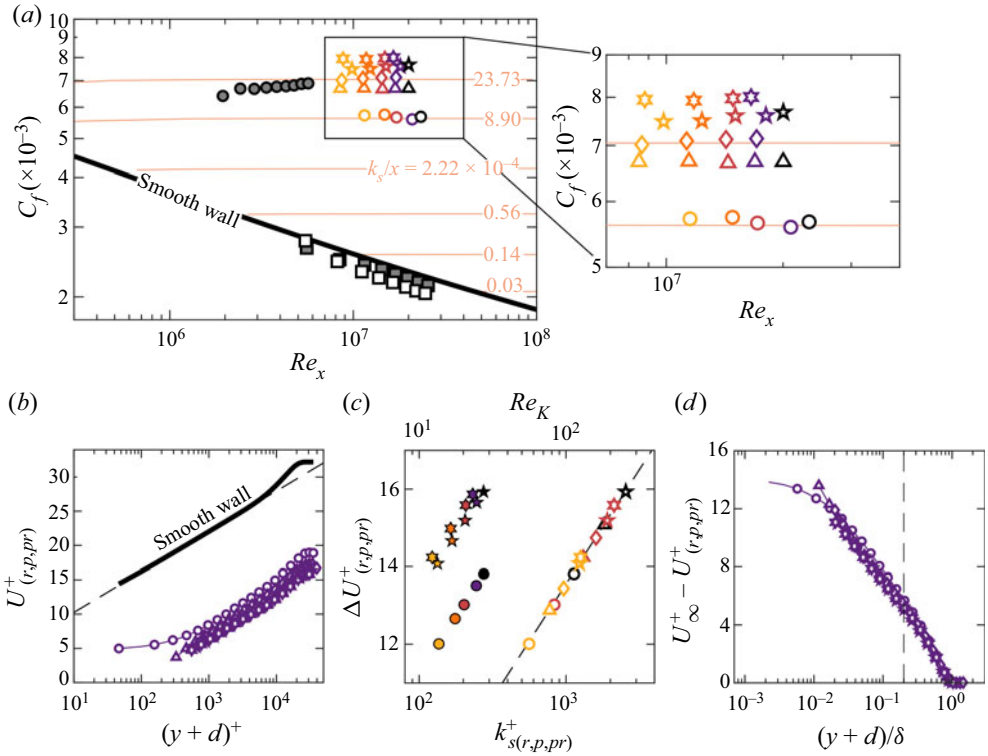

Figure 3. Panel (*a*) and inset: C_f as a function of Re_x for all test surfaces. Validation of the WSS measurements with smooth walls (□): fitted to the composite profile of Rodríguez-López, Bruce & Buxton (2015) (■) and the analytical solution of Monty *et al.* (2016) (▬). The same porous surface measured by Esteban *et al.* (2022) (●). Porous wall ($k_{s_p} = 7.83$ mm) at constant k_{s_p}/x (——, orange), obtained from Monty *et al.* (2016). Panel (*b*) shows U^+ as a function of $(y+d)^+$ for matched $Re_\tau \approx 27\,700$, - - - : $1/\kappa \ln(y+d)^+ + B$. Panel (*c*) shows ΔU^+ as functions of k_s^+ (white-filled symbols, bottom axis) for all test surfaces (subscripts '*p*', '*r*', and '*pr*') and Re_K (filled symbols, top axis) , - - - : $1/\kappa \ln k_s^+ + B - B_{FR}$. Legends are shown in table 1. (*d*) Velocity defect $U^+_\infty - U^+$ as a function of $(y+d)/\delta$ for matched $Re_\tau \approx 27\,700$. In (*b–d*), some data are downsampled for clarity.

surfaces are obtained by fitting the mean profile to a modified method of Rodríguez-López *et al.* (2015). The terms in (1.1), including ΔU^+, are fitted to minimise the error between the experimental data and a theoretical profile, with the exception of U_τ as it is obtained independently instead from direct WSS measurements. The fit yields $\kappa = 0.39$ and $B = 4.34 \pm 0.08$ (consistent with those obtained for TBLs developing over various porous walls measured by Esteban *et al.* 2022). The equivalent sand grain roughness for each test surface ($k_{s_{(p,r,pr)}}$) is obtained from the fitted $\Delta U^+_{(p,r,pr)}$ via (1.2) from the highest *Re* case listed in table 1, which has the longest logarithmic region. Porous wall C_f ('○' (yellow) to '○' (black) symbols in figure 3*a*) is compared to the analytical solution proposed by Monty *et al.* (2016) over constant $k_{s_p}/x = 8.9 \times 10^{-4}$ ($k_{s_p} = 7.83$ mm, within 2 % error from that obtained by Esteban *et al.* 2022). Additionally, C_f obtained by Esteban *et al.* (2022) for the same porous wall at lower x ('●' symbol in figure 3*a*) is also compared to the analytical solution ($k_{s_p}/x = 2.4 \times 10^{-3}$), both showing good agreement with these solutions. We note that the porous wall in this study has the pore size of $s^+ \geq 63$, above the threshold set by Breugem *et al.* (2006) ($\leq$5 viscous scaling in size, akin to the hydrodynamically smooth

https://doi.org/10.1017/jfm.2023.497 Published online by Cambridge University Press

condition) for full isolation of permeability effect. Present results in figure 3(*a*) show that for the baseline porous wall case *P* (without overlaying roughness *R*), C_f is invariant to *Re*, suggesting that the mechanism for skin friction drag here is dominated by blockage.

Figure 3(*b*) shows the vertical downward shift in the logarithmic region for all test surfaces at a matched $Re_\tau \approx 27\,700$ (the highest matched Re_τ for the *PR*2 set and second highest for *PR*1) from a smooth wall TBL at this matched Re_τ. This shift, denoted by $\Delta U^+_{(p,r,pr)}$, is shown as a function of $k^+_{s_{(p,r,pr)}}$ in figure 3(*c*) for all test surfaces (white-filled contours). The $k^+_{s_{(p,r,pr)}}$ are obtained from their respective fitted $\Delta U^+_{(p,r,pr)}$ via (1.2). All collapse to the logarithmic function $(1/\kappa)\ln k^+_{s_{(p,r,pr)}} + B - B_{FR}$ (1.2), although this is given since k_s is not obtained independently from ΔU^+. The magnitude of k_s^+ (figure 3*c*) exceeds the threshold defined by Flack & Schultz (2010), $k_s^+ \gtrsim 70$, ensuring that all test surfaces are fully rough and thus ΔU^+ depends solely on k_s. It should be noted that ΔU^+ here accounts for the total momentum deficit (from that of smooth wall TBLs) in both porous and rough walls, and it shows that it is possible to characterise porous walls with the same framework used for rough-wall characterisation (i.e. logarithmic shift that scales on k_s). The effect of permeability on ΔU^+ is shown in figure 3(*c*) for test surfaces comprising porous walls (*P*, *PR*1 and *PR*2, filled contours). Although it is clear that ΔU^+ is logarithmically scaled by Re_K, universality, as shown in figure 3(*c*) with k_s, is not apparent. This highlights the importance of accounting for the 'blockage' effect (1.6). At high range of Re_τ tested in this study, the outer-layer similarity is preserved for all test surfaces (i.e. velocity defect profiles collapse beyond $y/\delta \gtrsim 0.2$, figure 3*d*), ensuring that a given value of k_s (for each test surface) can be utilised to predict the drag at higher Reynolds numbers.

3. Decoupling permeability and roughness effect

3.1. *Additional blockage effect*

As a roughness interface is added overlaying the porous wall (case *PR*), (1.7) for porous walls may be written for the porous–rough walls as

$$k_{s_{pr}} = Re_K k_{s_{be}}, \tag{3.1}$$

where $k_{s_{be}}$ is the 'equivalent blockage' term for roughness overlaying porous walls, possibly a function of the characteristic length scale of the roughness (i.e. k_{s_r}) and the blockage of the porous substrate k_{s_b}. When two substrates have an approximately matched permeability, then the additional blockage effect can be approximated by $k_{s_{be}}/k_{s_b} \approx k_{s_{pr}}/k_{s_p}$. Case *PR*1 has five matched Re_K with case *P*. As the k_s for these surfaces are known from fitting ΔU^+ (§ 2.4), the additional blockage is approximated by $k_{s_{be}}/k_{s_b} \approx 2.25$. This is interpreted as the rough wall *R*1 increases the total blockage effect by approximately 2.25 times from that of the porous wall.

At this point, the empirical formulation of $k_{s_{be}}$ is unknown. Let the porous wall remain unchanged and the overlaying roughness effect be represented solely by the rough-wall characteristic length scale k_{s_r}:

$$k_{s_{be}} = k_{s_b} C k_{s_r}, \tag{3.2}$$

where *C* is a constant. For an approximately matched Re_K,

$$C \approx \frac{k_{s_{pr}}}{k_{s_p} k_{s_r}}. \tag{3.3}$$

https://doi.org/10.1017/jfm.2023.497 Published online by Cambridge University Press

We obtain $C = 0.17 \pm 5\,\%$ for case $PR1$ (range of C is estimated based on differences in matched Re_K), and further test this formulation for the second roughness $PR2$. Here, there are four matched Re_K cases (within 10 % difference, table 1). The total blockage effect increases by approximately 2.5 times from the porous wall (figure 3*e*), consistent with the increasing C_f of case $R2$ from that of $R1$ (figure 3*a*). The constant C appears to be similar to that obtained from $R1$, $C = 0.15 \pm 10\,\%$ (based on matched Re_K differences). This suggests that the formulation has the potential to be applicable across different cases and is not dependent on the type of roughness.

3.2. *Equivalent homogeneous roughness*

A recent study by Hutchins *et al.* (2023) suggested that in the fully rough regime, the drag coefficient C_D of a rough plate of length L is well-described by the power law, $C_D \propto (k_s/L)^n$. Further, for a heterogeneous rough wall (i.e. a rough wall constructed from various patches of homogeneous roughness of roughness length scale k_{s_i} covering an area A_i), the equivalent homogeneous roughness length k_{ehr} can be defined as

$$k_{ehr} = \left[\frac{1}{A}\sum_{i=1}^{N} k_{s_i}^n A_i\right]^{1/n} \quad \text{where } A = \sum_{i=1}^{N} A_i. \tag{3.4}$$

In the present study, the drag penalty from all test surfaces can be represented by the logarithmic shift ΔU^+ (figure 3*b*), suggesting the possibility of characterising permeable walls with the same framework used for rough-wall TBLs. Thus, we might consider porous–rough walls as simply a combination of two 'homogeneous roughnesses' of the same coverage area overlaying each other. This also assumes that the two different roughness are 'sparse' and the superposition does not lead to new physical mechanisms that alter the momentum deficit. In this scenario, (3.4) is reduced to

$$k_{s_{pr}} = [k_{s_p}^n + k_{s_r}^n]^{1/n}. \tag{3.5}$$

For case $PR1$, n is obtained by solving (3.5) with the known k_s for each $PR1$, P and $R1$, resulting in $n = 1.42$. The same approach is applied to case $PR2$, resulting in $n = 1.54$, which is relatively consistent with that obtained from case $PR1$.

It is still unknown, at this point, what the empirical formulation for the roughness effect is. Present results suggest that it is possibly in terms of an additional logarithmic shift similar to (1.6). Further, it is still unclear what the empirical relation with the characteristic length scale of roughness (rough wall k_s) is. For the two methods tested in § 3, it is neither understood what the physical interpretations of constants C and n are, nor whether these constants are universal for various types of rough walls. We are unable to answer these questions in this study due to the limited number of test surfaces. However, present results suggest a promising start towards decoupling permeability and roughness effects.

4. Conclusions and future work

We conduct velocity and drag measurements of TBLs developing over various porous–rough wall combinations, with the roughness effect systematically varied while maintaining the permeability effect. Measurements are conducted at relatively high Reynolds numbers($14\ 400 \leq Re_\tau \leq 33\ 100$), with a set of matched Re_τ (within 10 %) and Re_K ($13 \leq Re_K \leq 27.5$) of each porous–rough combinations. Present results suggest that the increase in drag over porous, rough, and porous–rough walls is characterised

https://doi.org/10.1017/jfm.2023.497 Published online by Cambridge University Press

by a downward shift in the logarithmic region ΔU^+ from that of smooth wall TBLs and that the mean flow follows outer-layer similarity for cases examined at these high Reynolds numbers (with substantial scale separation). Further analysis shows that ΔU^+ from these surfaces can be characterised by the roughness length scale k_s, suggesting the possibility of characterising porous walls with the same framework used for rough-wall TBLs. Following the hypothesis of Esteban *et al.* (2022) and the surfaces tested in the present study, it is viable that for a porous–rough wall, permeability and roughness effects are represented by Re_K and an equivalent blockage function, respectively, with the equivalent blockage consisting of the blockage effect from the porous substrate and additional roughness interface above the porous wall. Present results suggest that the rough walls increase the blockage of porous–rough walls by approximately 2.3–2.5 times from that of the porous wall for both roughnesses tested in this study. We observed that the additional roughness effect follows Ck_{s_r}, where constant $C \approx 0.16$ for both rough-wall test surfaces. Analysis of the same data with the method suggested by Hutchins *et al.* (2023) shows that the effect of porous and rough walls may be decoupled using an area-weighted power-mean (with $n \approx 1.5$ for both surfaces) to obtain an equivalent roughness length for both rough-wall test surfaces. The empirical formulation as well as the physical interpretation of constants observed in this study requires further data (especially with walls with a wide range of permeabilities) and should be the focus of future work. This is perhaps best achieved using numerical simulations where the permeabilities can be potentially altered by varying the boundary conditions.

Supplementary material. Data published in this article are available on the University of Southampton repository (DOI: 10.5258/SOTON/D2670).

Funding. We gratefully acknowledge the financial support from EPSRC (grant ref no. EP/S013296/1) and the European Office for Airforce Research and Development (grant no. FA9550-19-1-7022, Programme Manager: Dr D. Smith). P.J. acknowledges the financial support from UKRI Postdoc Guarantee (grant ref no. EP/X032590/1).

Declaration of interest. The authors declare no conflict of interest.

Author ORCIDs.
D.D. Wangsawijaya https://orcid.org/0000-0002-7072-4245;
P. Jaiswal https://orcid.org/0000-0002-5240-9911;
B. Ganapathisubramani https://orcid.org/0000-0001-9817-0486.

Author contributions. P.J. and D.D.W. designed, carried out measurements, and postprocessed the data. D.D.W. analysed the data and wrote the manuscript. B.G. was responsible for conceptualisation, funding acquisition, editing of drafts and project management.

References

Breugem, W.P., Boersma, B.J. & Uittenbogaard, R.E. 2006 The influence of wall permeability on turbulent channel flow. *J. Fluid Mech.* **562**, 35–72.

Efstathiou, C. & Luhar, M. 2018 Mean turbulence statistics in boundary layers over high-porosity foams. *J. Fluid Mech.* **841**, 351–379.

Esteban, L.B., Rodríguez-López, E., Ferreira, M.A. & Ganapathisubramani, B. 2022 Mean flow of turbulent boundary layers over porous substrates. *Phys. Rev. Fluids* **7** (9), 094603.

Flack, K.A. & Schultz, M.P. 2010 Review of hydraulic roughness scales in the fully rough regime. *J. Fluids Engng* **132** (4), 041203.

Hahn, S., Je, J. & Choi, H. 2002 Direct numerical simulation of turbulent channel flow with permeable walls. *J. Fluid Mech.* **450**, 259–285.

Hama, F.R. 1954 Boundary layer characteristics for smooth and rough surfaces. *Trans. Soc. Nav. Archit. Mar. Engrs* **62**, 333–358.

https://doi.org/10.1017/jfm.2023.497 Published online by Cambridge University Press

HUTCHINS, N., GANAPATHISUBRAMANI, B., SCHULTZ, M.P. & PULLIN, D.I. 2023 Defining an equivalent homogeneous roughness length for turbulent boundary layers developing over patchy or heterogeneous surface. *Ocean Engng* **271**, 113454.

HUTCHINS, N., NICKELS, T.B., MARUSIC, I. & CHONG, M.S. 2009 Hot-wire spatial resolution issues in wall-bounded turbulence. *J. Fluid Mech.* **635**, 103–136.

KONG, F. & SCHETZ, J. 1982 Turbulent boundary layer over porous surfaces with different surface geometries. In *the 20th AIAA Aerospace Sciences Meeting*. AIAA.

LIGRANI, P.M. & BRADSHAW, P. 1987 Subminiature hot-wire sensors: development and use. *J. Phys.* E*: Sci. Instrum.* **20**, 323–332.

LUHAR, M., ROMINGER, J. & NEPF, H. 2008 Interaction between flow, transport and vegetation spatial structure. *Environ. Fluid Mech.* **8**, 423–439.

MANES, C., POGGI, D. & RIDOLFI, L. 2011 Turbulent boundary layers over permeable walls: scaling and near-wall structure. *J. Fluid Mech.* **687**, 141–170.

MANES, C., POKRAJAC, D., MCEWAN, I. & NIKORA, V. 2009 Turbulence structure of open channel flows over permeable and impermeable beds: a comparative study. *Phys. Fluids* **21**, 125109.

MONTY, J.P., DOGAN, E., HANSON, R., SCARDINO, A.J., GANAPATHISUBRAMANI, B. & HUTCHINS, N. 2016 An assessment of the ship drag penalty arising from light calcareous tubeworm fouling. *Biofouling* **32** (4), 451–464.

NIKURADSE, J. 1933 Strömungsgesetze in rauhen rohren. *VDI Forschungsheft* 361 (translation in 1950 Laws of flow in rough pipes. *NACA Tech. Mem.* 1292).

RAUPACH, M.R. 1992 Drag and drag partition on rough surfaces. *Boundary-Layer Meteorol.* **60**, 375–395.

RODRÍGUEZ-LÓPEZ, E., BRUCE, P.J.K. & BUXTON, O.R.H. 2015 A robust post–processing method to determine skin friction in turbulent boundary layers from the velocity profile. *Exp. Fluids* **56**, 68.

ROSTI, M.E., CORTELEZZI, L. & QUADRIO, M. 2015 Direct numerical simulation of turbulent channel flow over porous walls. *J. Fluid Mech.* **784**, 396–442.

SHARMA, A. & GARCÍA-MAYORAL, R. 2020 Turbulent flows over dense filament canopies. *J. Fluid Mech.* **888**, A2.

SHIMIZU, Y., TSUJIMOTO, T. & NAKAGAWA, H. 1990 Experiment and macroscopic modelling of flow in highly permeable porous medium under free-surface flow. *J. Hydrosci. Hydraul. Engng* **8** (1), 69–78.

SUGA, K., MATSUMURA, Y., ASHITAKA, Y., TOMINAGA, S. & KANEDA, M. 2010 Effects of wall permeability on turbulence. *Intl J. Heat Fluid Flow* **31**, 974–984.

TANINO, Y. & NEPF, H. 2008 Laboratory investigation of mean drag in a random array of rigid, emergent cylinders. *J. Hydraul. Engng ASCE* **134** (1), 34–41.

ZAGNI, A.F.E. & SMITH, K.V.H. 1976 Channel flow over permeable beds of graded spheres. *J. Hydraul. Div. ASCE* **102** (2), 207–222.

ZIPPE, H.J. & GRAF, W.H. 1983 Turbulent boundary-layer flow over permeable and non-permeable rough surfaces. *J. Hydraul. Res.* **21** (1), 51–65.

https://doi.org/10.1017/jfm.2023.497 Published online by Cambridge University Press